IOP Publishing
Smart Materials and Structures
Smart Mater. Struct. **29** (2020) 085053 (15pp)
https://doi.org/10.1088/1361-665X/ab90a2

Experimentally validated model and power optimization of a magnetoelectric wireless power transfer system in free-free configuration

Binh Duc Truong and Shad Roundy

Department of Mechanical Engineering, University of Utah, 1495 E. 100 S., 1550 MEK, Salt Lake City, Utah, 84112, United States of America

E-mail: Binh.D.Truong@utah.edu

Received 19 February 2020, revised 13 April 2020
Accepted for publication 6 May 2020
Published 21 July 2020

Abstract

This article presents a thorough analysis and an equivalent circuit model of a wireless power transfer system utilizing magnetoelectric (ME) effects. Based on two-port theory, explicit analytical solutions of, (i) the ME coefficient α_{ME} (defined by the derivative of the generated electric field with respect to the applied magnetic field), and (ii) the power transferred to a load resistance, are derived and rigorously validated by experiments. The compact closed-forms of the optimal load and its corresponding maximum output power are developed. In our particular experimental system, a power of $\sim$10 mW is attained at an applied magnetic flux density of 318.9 μT with a laminated composite made by two Galfenol and one PZT layers. While α_{ME} is widely used in the literature as a standard criterion to evaluate the performance of a ME transducer, we reveal that larger α_{ME} does not always ensure higher optimum power delivered to the load. Instead, we quantify the essential influences of each magnetostrictive and piezoelectric phases on the maximum obtainable power. We show that the transduction factor between the magnetic and mechanical domains is often more critical for power optimization than the mechanical-electrical transduction factor as it determines and limits the maximum power available for transfer to a resistive load.

Keywords: wireless power transfer, magneto-electric effect, longitudinal vibration, equivalent circuit model, power optimization

(Some figures may appear in colour only in the online journal)

1. Introduction

Wireless power transfer (WPT) with a focus on biomedical applications has received significant attention recently as it provides the promise of a safe approach to deliver power to implantable medical devices (IMDs). Resonant inductive coupling (RIC) wireless power transfer systems (WPTS) are perhaps the most prevalent technology to realize this vision. However, as the size of IMDs decreases, RIC systems may be less successful because of the need to operate at high frequency, which results in high attenuation in soft tissue. In addition, subject to the International Commission on Non-Ionizing Radiation Protection (ICNIRP) Safety Standards [1, 2], the maximum allowable amplitude of the magnetic flux density (i.e. **B**−field) that can be applied to humans is restricted by the driving frequency. For example, largest permissible **B**−field at 6.78 MHz is 0.29 μT whereas at 100 kHz it is 100 μT. These safety constraints reduce the potential of RIC approach when applied to very small biomedical systems.

Low-frequency near-field techniques are attractive alternatives to RIC for powering biomedical devices. Electrodynamic (ED) and Magneto-Mechano-Electric (MME) WPT systems were proposed and thoroughly investigated, including both linear and rotational vibration [3–6]. In these mechanisms, either

 © 2020 IOP Publishing Ltd Printed in the UK

an electromagnetic transducer or a piezoelectric generator along with one or more permanent magnets form a receiver. Meanwhile, a coil or a rotation magnet is utilized as a transmitter. Typical operating frequencies of the ED and MME devices are well below 1 kHz, which allows the application of a maximum $\mathbf{B}-$field of $\sim$2 mT [7]. A disadvantage of these structures is a relatively low efficiency due to the weak coupling between the magnetic and mechanical domains that is realized by the interaction of magnet and magnetic field. Moreover, the magnetic-to-mechanical transduction factor, and therefore, the maximum possible power transferred to an electrical load, depends on the magnet volume. Given the fact that implantable integrated systems are desired to be as small as possible, the required use of permanent magnets may be challenging in the miniaturization of implants.

Mid-field and far-field electromagnetic WPT systems (referred to here as RF WPTS) have been widely employed to power pacemakers [8–10]. However, this technique can induce significant heating caused by RF wave absorption in the human body. This absorption both reduces system efficiency and can pose a health risk to users. According to the ICNIRP regulation [1, 11], the maximum specific absorption rate (SAR) is set to be 2 W/kg per 10 g of tissue in order to avoid the safety risk that these systems could pose.

Acoustic power transfer is another possible solution, whose advantages include lower absorption and shorter wavelength enabling smaller transducers [12]. However, the acoustic transmitter must be in direct contact with the skin, and the transmission of acoustic power through the bone seems to be minimal since the large acoustic impedance mismatch between soft tissue and bone results in most of the acoustic energy being reflected.

With the limitations of the available WPT technologies (including ED, MME, RIC, RF, and ultrasonic waves) pointed out, we are seeking another approach for powering biomedical implantable electronics that is able to overcome those obstacles. A mechanism that operates at low frequency with an acceptable transfer efficiency is considered appropriate. We believe that a WPTS utilizing the magnetoelectric (ME) effects possesses such potential.

Advances in ME multiferroic materials have triggered significant research interest [13]. With a shift of focus from fundamental material discoveries to translational research, the field of multiferroics and magnetoelectrics is anticipated to make further application-oriented breakthroughs over the next few years [14]. The recent development of a ME antenna indicated that for a given frequency its wavelength could be five orders of magnitude shorter than the electromagnetic wavelength, leading to possibly dramatic miniaturization [15]. Furthermore, the typical operating frequency of ME systems is relatively low, in the range of tens of kHz, which enables higher permissible applied $\mathbf{B}-$field than that of RIC WPTS [1]. These characteristics make ME generator a promising alternative to other WPT technologies, especially for IMDs.

The concept of a ME effect was first introduced by Röntgen in 1888 with his discovery that a dielectric material could be magnetized under a magnetic field [16]. In the next 100 years, various ME architectures and materials have been discovered and studied, with most studies focused on single-phase and two-phase ME composites [17, 18]. In 2001, Ryu *et al* proposed a ME laminated composite combined by two radial-magnetized Terfernol-D and one thickness-polarized PZT disks [19]. Since then, laminated structures have become preferable due to their strong ME coupling, and high reproducibility and reliability. A significant modeling effort which captures the performance of ME transducers was undertaken by Dong *et al*, in which the ME effect was described by an equivalent circuit model [20, 21]. However, the authors were only concerned with the open-circuit voltage for a sensing system. The actual power transferred to a load at a given external $\mathbf{B}-$field was not addressed.

ME laminated composites have been widely utilized in many applications, such as magnetic field sensors [22–24], ME Random Access Memory (MERAM) [25–27] and electronic components [28–30]. However, its potential in WPT has not been thoroughly explored. To the authors' knowledge, this work is one of the first efforts to utilize a laminated composite ME-transducer as a receiver for a WPTS, adding to the efforts of [31, 32]. In this article, we further develop a linear two-port model of a ME-based WPTS, together with corrections to essential errors found in [20]. The model is experimentally validated, which is then used for analyzing a figure of merit and the fundamental performance limits of the architecture under consideration. A standard criterion to evaluate the ME effect is the ME coefficient (denoted as α_{ME}) defined by the rate of change of the electric field in response to the applied magnetic field. Most studies in the literature so far have indicated a significant advantage in obtaining α_{ME} as high as possible [33–35]. While this statement may hold true for magnetic field sensing devices, it is still questionable for a WPTS. Clarifying this issue is also one of the central objectives of the paper.

2. Mathematical analysis and essential equations

As shown in figure 1, we consider a ME laminated composite with two constituent materials, magnetostrictive and piezoelectric, bonded together by conductive epoxy. The piezoelectric and magnetostrictive phases are poled and magnetized in the thickness and length directions, respectively. The global coordinates of the beam are denoted by (x, y, z). Local coordinates of each layer are also included, where $3-$axis is always parallel to the polarization and magnetization vectors, $\overrightarrow{P}$ and $\overrightarrow{M}$. L and w are the length and width of the ME generator. t_{p} and t_{m} accordingly represent the thicknesses of the magnetostrictive and piezoelectric layers. In order to evaluate the transferred power capability, the output port of the ME transducer is connected to a resistor R_{L}, for the convenience and simplification. When an external AC magnetic field H_{ac} is applied along the longitudinal axis of the laminate, $(\overrightarrow{H_{\mathrm{ac}}} \parallel \overrightarrow{M}) \perp \overrightarrow{P}$, a strain is excited in the two magnetostrictive phases, which is then transferred to the piezoelectric layer through an interface coupling. As a result, the laminated composite vibrates in the $z-$direction.

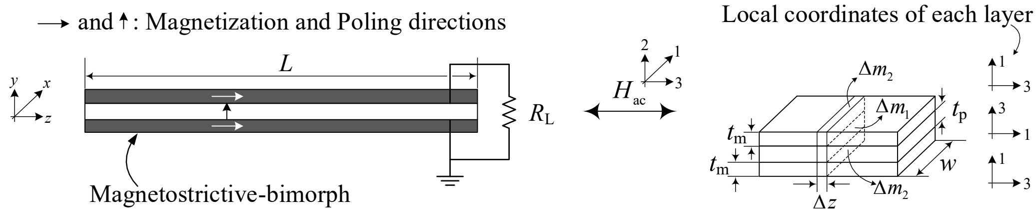

Figure 1. Schematic of ME transducers and geometric dimensions of the laminated composite.

The piezoelectric constitutive equations for the thickness poling are

$$S_{1\mathrm{p}} = s_{11}^{\mathrm{E}} T_{1\mathrm{p}} + d_{31,\mathrm{p}} E_3, \tag{1}$$

$$D_3 = d_{31,\mathrm{p}} T_{1\mathrm{p}} + \epsilon_{33}^{\mathrm{T}} E_3 \tag{2}$$

where $T_{1\mathrm{p}}$ and $S_{1\mathrm{p}}$ are the stress and strain of the piezoelectric layer imposed by the magnetostrictive layer, D_3 and E_3 are the electric displacement and electric field in the piezoelectric layer along z, respectively, s_{11}^{E} is the elastic compliance of the piezoelectric material under constant electric field E, $d_{31,\mathrm{p}}$ is the transverse electric constant and $\epsilon_{33}^{\mathrm{T}}$ is the dielectric permittivity under constant stress T.

The magnetostrictive constitutive equations for the longitudinal strain $S_{3\mathrm{m}}$ and the magnetic field flux density B_3 are

$$S_{3\mathrm{m}} = s_{33}^{\mathrm{H}} T_{3\mathrm{m}} + d_{33,\mathrm{m}} H_3, \tag{3}$$

$$B_3 = d_{33,\mathrm{m}} T_{3\mathrm{m}} + \mu_{33,\mathrm{m}}^{\mathrm{T}} H_3 \tag{4}$$

where H_3 is the AC applied magnetic field (i.e. H_{ac} in figure 1), $T_{3\mathrm{m}}$ is the stress in the magnetostrictive layer, s_{33}^{H} is the elastic compliance at constant H, $d_{33,\mathrm{m}}$ is the piezomagnetic constant and $\mu_{33,\mathrm{m}}^{\mathrm{T}}$ is the magnetic permeability at constant stress T.

Assume that an applied magnetic field H_3 is sinusoidal with angular frequency ω (e.g. $H_3 = H_0 \cos(\omega t)$), the corresponding vibration of the laminate is a harmonic motion along the longitudinal direction z. We denote (i) the displacements of the piezoelectric and magnetostrictive mass units (Δm_1 and $2\Delta m_2$) in the laminate are $u_{1\mathrm{p}}(z)$ and $u_{3\mathrm{m}}(z)$ respectively, and (ii) the corresponding strain components along z are

$$S_{1\mathrm{p}} = \partial u_{1\mathrm{p}} / \partial z, \tag{5}$$

$$S_{3\mathrm{m}} = \partial u_{3\mathrm{m}} / \partial z. \tag{6}$$

Here, in the same manner as in [36–39], we introduce an interface coupling coefficient, $0 \leq \kappa \leq 1$, which relates the strain transfer between the two phases (magnetostrictive and piezoelectric) such that $S_{1\mathrm{p}} = \kappa S_{3\mathrm{m}}$, and therefore $u_{1\mathrm{p}} = \kappa u_{3\mathrm{m}}$. With the presence of κ, all of the following derivations are, in general, different from the well-known results established in the literature [20, 40, 41], in which the authors only considered the ideal case $\kappa = 1$.

Based on the Newton's second law, the equation of motion of the laminate is given by

$$\Delta m_1 \frac{\partial^2 u_{1\mathrm{p}}}{\partial t^2} + 2\Delta m_2 \frac{\partial^2 u_{3\mathrm{m}}}{\partial t^2} = \Delta T_{1\mathrm{p}} A_1 + 2\Delta T_{3\mathrm{m}} A_2 \tag{7}$$

where

$$\Delta m_1 = \rho_{\mathrm{p}} A_1 \Delta z, \, \Delta m_2 = \rho_{\mathrm{m}} A_2 \Delta z, \tag{8}$$

$$A_1 = t_{\mathrm{p}} w, A_2 = t_{\mathrm{m}} w. \tag{9}$$

ρ_{p} and ρ_{m} are the mass densities of the piezoelectric and the magnetostrictive layers respectively. The geometric definitions of Δm_1, Δm_2, w, Δz, t_{p} and t_{m} are shown in figure 1. Considering an element of infinitesimal length, $\Delta z \to 0$, and with notice that $\partial^2 u_{3\mathrm{m}} / \partial t^2 = (\partial^2 u_{1\mathrm{p}} / \partial t^2) / \kappa$, equation (7) can be re-written as

$$\overline{\rho} \frac{\partial^2 \mathrm{u}}{\partial t^2} = n \frac{\partial T_{1\mathrm{p}}}{\partial z} + (1-n) \frac{\partial T_{3\mathrm{m}}}{\partial z} \tag{10}$$

where the variable of interest is $u = u_{1\mathrm{p}}$,

$$n = \frac{A_1}{A_1 + 2A_2} = \frac{t_{\mathrm{p}}}{t_{\mathrm{p}} + 2t_{\mathrm{m}}}, 0 < n < 1, \tag{11}$$

$$\overline{\rho} = \frac{\rho_{\mathrm{p}} A_1 + 2\rho_{\mathrm{m}} A_2 / \kappa}{A_1 + 2A_2}. \tag{12}$$

Based on the piezoelectric constitutive equations, the partial derivative of the stress with respect to the position in the length direction is computed as

$$\frac{\partial T_{1\mathrm{p}}}{\partial z} = \left(s_{11}^{\mathrm{E}} - \frac{d_{31,\mathrm{p}}^2}{\epsilon_{33}^{\mathrm{T}}} \right)^{-1} \left(\frac{\partial S_{1\mathrm{p}}}{\partial z} - \frac{d_{31,\mathrm{p}}}{\epsilon_{33}^{\mathrm{T}}} \frac{\partial D_3}{\partial z} \right), \tag{13}$$

$$\frac{\partial T_{3\mathrm{m}}}{\partial z} = \left(s_{33}^{\mathrm{H}} - \frac{d_{33,\mathrm{m}}^2}{\mu_{33,\mathrm{m}}^{\mathrm{T}}} \right)^{-1} \left(\frac{\partial S_{3\mathrm{m}}}{\partial z} - \frac{d_{33,\mathrm{m}}}{\mu_{33,\mathrm{m}}^{\mathrm{T}}} \frac{\partial B_3}{\partial z} \right). \tag{14}$$

It should be noted that, the constitutive equations of piezoelectric and magnetostrictive materials are written under the assumption that all field components do not vary through the width and thickness directions, which means

$\partial D_1/\partial x = \partial D_2/\partial y = 0$ and $\partial B_1/\partial x = \partial B_2/\partial y = 0$. In addition, Maxwell's magnetostatic and electrostatic equations in magnetostrictive and piezoelectric materials (also known as Gauss's laws for magnetism) are given by

$$\mathrm{rot}\ \vec{E} = 0, \mathrm{div}\vec{D} = 0, \tag{15}$$

$$\mathrm{div}\vec{B} = 0, \mathrm{rot}\ \vec{H} = 0. \tag{16}$$

Hence $\partial D_3/\partial z = 0$ and $\partial B_3/\partial z = 0$. Equations (13) and (14) now become

$$\frac{\partial T_{1\mathrm{p}}}{\partial z} = \left(s_{11}^{\mathrm{E}} - \frac{d_{31,\mathrm{p}}^2}{\epsilon_{33}^{\mathrm{T}}}\right)^{-1} \frac{\partial^2 \mathrm{u}}{\partial z^2} = \frac{1}{s_{11}^{\mathrm{D}}} \frac{\partial^2 \mathrm{u}}{\partial z^2}, \tag{17}$$

$$\frac{\partial T_{3\mathrm{m}}}{\partial z} = \left(s_{33}^{\mathrm{H}} - \frac{d_{33,\mathrm{m}}^2}{\mu_{33,\mathrm{m}}^{\mathrm{T}}}\right)^{-1} \frac{1-n}{\kappa} \frac{\partial^2 \mathrm{u}}{\partial z^2} = \frac{1-n}{\kappa s_{33}^{\mathrm{B}}} \frac{\partial^2 \mathrm{u}}{\partial z^2}. \tag{18}$$

By substituting (17) and (18) into (10), the motion equation can be written

$$\frac{1}{\bar{v}^2} \frac{\partial^2 \mathrm{u}}{\partial t^2} = \frac{\partial^2 \mathrm{u}}{\partial z^2} \tag{19}$$

where

$$\bar{v}^2 = \frac{1}{\bar{\rho}}\left[n\left(s_{11}^{\mathrm{E}} - \frac{d_{31,\mathrm{p}}^2}{\epsilon_{33}^{\mathrm{T}}}\right)^{-1} + \frac{1-n}{\kappa}\left(s_{33}^{\mathrm{H}} - \frac{d_{33,\mathrm{m}}^2}{\mu_{33,\mathrm{m}}^{\mathrm{T}}}\right)^{-1}\right]$$
$$= \frac{1}{\bar{\rho}}\left(\frac{n}{s_{11}^{\mathrm{D}}} + \frac{1-n}{\kappa s_{33}^{\mathrm{B}}}\right). \tag{20}$$

The expression of $\bar{v}^2$ is slightly different from the formula presented by Dong *et al* [20], since the authors neither took Maxwell's equations into consideration nor the effects of the electric field E_3 and the magnetic flux density B_3 on the strains $S_{1\mathrm{p}}$ and $S_{3\mathrm{m}}$ respectively. Only in the cases where $s_{11}^{\mathrm{D}} \approx s_{11}^{\mathrm{E}}$, $s_{33}^{\mathrm{B}} \approx s_{33}^{\mathrm{H}}$ and $\kappa = 1$, (17) and (18) recover the equations reported in [20].

Under harmonic motion, the general solution of the one-dimensional wave equation (19) in the time domain is

$$u(z,t) = Y(z)T(t), \tag{21}$$

$$Y(z) = A\cos(kz) + B\sin(kz), \tag{22}$$

$$T(t) = C\cos(\omega t) + D\sin(\omega t) \tag{23}$$

where the squared wave number is defined as

$$k^2 = \frac{\omega^2}{\bar{v}^2}. \tag{24}$$

The real constants A and B are determined by boundary conditions, while C and D depends on initial conditions. Solving for $\{A, B, C, D\}$ is not the objective of this paper, however, this time-domain solution is a preliminary step for further analysis in the frequency domain in the following sections.

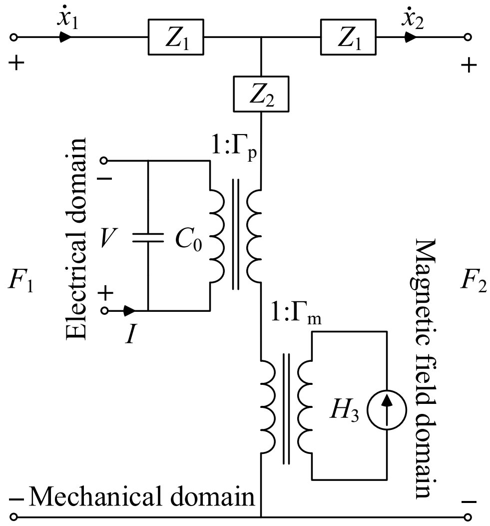

Figure 2. Equivalent circuit model of magnetoelectric wireless power transfer system.

3. Equivalent two-port model

The linear two-port network is one of the most widely used models for ED, MME, and RIC WPT systems. Under the right circumstances (e.g. small vibration amplitude or single transmitter-receiver configuration), it is a convenient method of describing dynamical characteristics and interpreting the fundamental performance without compromising the accuracy of the model. The main aim of this section is to simplify a multi-port model of the original system when configured in the free-free condition and develop its two-port equivalent circuit.

The driving frequency of WPT systems can be controlled at the transmitter side. Therefore, investigating and optimizing the frequency responses of the system is of great interest. In order to avoid any possible misunderstanding that might arise for the readers, frequency-domain variables are denoted with a hat on top of a character rather than using the same notations for both the time and frequency domains as seen in [20, 21]. From this point on, all the derivations are carried out in the frequency domain, unless stated explicitly.

The complex amplitude of the displacement, $\widehat{X}$, is a function of z only, $\widehat{X}(z) = Y(z)$ where $Y(z)$ is given in (22). The boundary conditions given in terms of the face velocities of the composite laminate (denoted as $\widehat{V}_1$ and $\widehat{V}_2$) are

$$\widehat{V}_1|_{z=0} = j\omega\widehat{X}(0) = j\omega A, \tag{25}$$

$$\widehat{V}_2|_{z=L} = j\omega\widehat{X}(L) = j\omega\big(A\cos(kL) + B\sin(kL)\big), \tag{26}$$

Assuming that the boundary conditions $\widehat{V}_1$ ($\widehat{V}_2$) at $z = 0$ ($z = L$) were determined, two constant coefficients A (B) and the complex amplitude of the displacement are computed as

$$A = \frac{\widehat{V}_1}{j\omega}, \tag{27}$$

$$B = \frac{\widehat{V}_2 - \widehat{V}_1 \cos(kL)}{j\omega \sin(kL)}, \tag{28}$$

$$\widehat{X}(z) = \frac{\widehat{V}_1}{j\omega} \cos(kz) + \frac{\widehat{V}_2 - \widehat{V}_1 \cos(kL)}{j\omega \sin(kL)} \sin(kz). \tag{29}$$

The complex amplitude of the strains at the faces are

$$\widehat{S}_{1\mathrm{p}}(0) = \frac{\mathrm{d}\widehat{X}}{\mathrm{d}z}\Big|_{z=0} = \frac{\widehat{V}_2 - \widehat{V}_1 \cos(kL)}{j\overline{v} \sin(kL)}, \tag{30}$$

$$\widehat{S}_{1\mathrm{p}}(L) = \frac{\mathrm{d}\widehat{X}}{\mathrm{d}z}\Big|_{z=L} = \frac{\widehat{V}_2 \cos(kL) - \widehat{V}_1}{j\overline{v} \sin(kL)}, \tag{31}$$

$$\widehat{S}_{3\mathrm{m}}(0) = \frac{1}{\kappa}\widehat{S}_{1\mathrm{p}}(0), \widehat{S}_{3\mathrm{m}}(L) = \frac{1}{\kappa}\widehat{S}_{1\mathrm{p}}(L). \tag{32}$$

The corresponding forces related to the face stresses are

$$\begin{aligned}
\widehat{F}_1 &= -A_1 \widehat{T}_{1\mathrm{p}}|_{z=0} - 2A_2 \widehat{T}_{3\mathrm{m}}|_{z=0} \\
&= -A_1 \frac{1}{s_{11}^{\mathrm{E}}} \left(\widehat{S}_{1\mathrm{p}}(0) - d_{31,\mathrm{p}}\widehat{E}_3\right) - 2A_2 \frac{1}{s_{33}^{\mathrm{H}}} \left(\widehat{S}_{3\mathrm{m}}(0) - d_{33,\mathrm{m}}\widehat{H}_3\right) \\
&= -\left(\frac{A_1}{s_{11}^{\mathrm{E}}} + \frac{1}{\kappa}\frac{2A_2}{s_{33}^{\mathrm{H}}}\right) \frac{\widehat{V}_2 - \widehat{V}_1 \cos(kL)}{j\overline{v} \sin(kL)} + \frac{A_1 d_{31,\mathrm{p}}}{s_{11}^{\mathrm{E}}}\widehat{E}_3 + \frac{2A_2 d_{33,\mathrm{m}}}{s_{33}^{\mathrm{H}}}\widehat{H}_3,
\end{aligned} \tag{33}$$

$$\begin{aligned}
\widehat{F}_2 &= -A_1 \widehat{T}_{1\mathrm{p}}|_{z=L} - 2A_2 \widehat{T}_{3\mathrm{m}}|_{z=L} \\
&= -A_1 \frac{1}{s_{11}^{\mathrm{E}}} \left(\widehat{S}_{1\mathrm{p}}(L) - d_{31,\mathrm{p}}\widehat{E}_3\right) - 2A_2 \frac{1}{s_{33}^{\mathrm{H}}} \left(\widehat{S}_{3\mathrm{m}}(L) - d_{33,\mathrm{m}}\widehat{H}_3\right) \\
&= -\left(\frac{A_1}{s_{11}^{\mathrm{E}}} + \frac{1}{\kappa}\frac{2A_2}{s_{33}^{\mathrm{H}}}\right) \frac{\widehat{V}_2 \cos(kL) - \widehat{V}_1}{j\overline{v} \sin(kL)} + \frac{A_1 d_{31,\mathrm{p}}}{s_{11}^{\mathrm{E}}}\widehat{E}_3 + \frac{2A_2 d_{33,\mathrm{m}}}{s_{33}^{\mathrm{H}}}\widehat{H}_3.
\end{aligned} \tag{34}$$

The coupling voltage $\widehat{V}$ produced at the two surfaces of the piezoelectric layer is determined as

$$\widehat{V} = \int_0^{t_\mathrm{p}} \widehat{E}_3 \mathrm{d}y = \widehat{E}_3 t_\mathrm{p} \tag{35}$$

where y is the thickness direction. The forces $\widehat{F}_1$ and $\widehat{F}_2$ in (33) and (34) now can be rewritten as follows

$$\widehat{F}_1 = Z_1\widehat{V}_1 - \left(\widehat{V}_2 - \widehat{V}_1\right)Z_2 - \Gamma_\mathrm{p}\widehat{V} + \Gamma_\mathrm{m}\widehat{H}_3, \tag{36}$$

$$\widehat{F}_2 = -Z_1\widehat{V}_2 - \left(\widehat{V}_2 - \widehat{V}_1\right)Z_2 - \Gamma_\mathrm{p}\widehat{V} + \Gamma_\mathrm{m}\widehat{H}_3 \tag{37}$$

where Z_1 and Z_2 are referred to the mechanical characteristic impedances, Γ_p is the electromechanical transduction factor of the piezoelectric layer and Γ_m is the magneto-elastic (also known as electrodynamic) transduction factor of the magnetostrictive layer. These parameters are given by

$$Z_1 = -\left(\frac{n}{s_{11}^{\mathrm{E}}} + \frac{1-n}{\kappa s_{33}^{\mathrm{H}}}\right)\frac{A \tan(kL/2)}{j\overline{v}}, \tag{38}$$

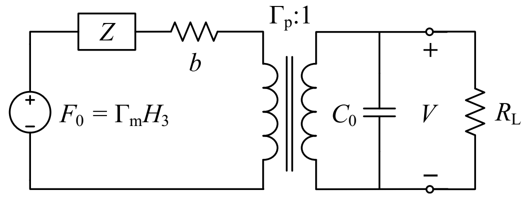

Figure 3. Simplified model with free-free conditions.

$$Z_2 = \left(\frac{n}{s_{11}^{\mathrm{E}}} + \frac{1-n}{\kappa s_{33}^{\mathrm{H}}}\right)\frac{A}{j\overline{v}\sin(kL)}, \tag{39}$$

$$\Gamma_\mathrm{p} = -\frac{A_1 d_{31,\mathrm{p}}}{t_\mathrm{p} s_{11}^{\mathrm{E}}} = -w\frac{d_{31,\mathrm{p}}}{s_{11}^{\mathrm{E}}}, \tag{40}$$

$$\Gamma_\mathrm{m} = 2wt_\mathrm{m}\frac{d_{33,\mathrm{m}}}{s_{33}^{\mathrm{H}}}. \tag{41}$$

The piezoelectric constant $d_{31,\mathrm{p}}$ is usually a negative number, thus $\Gamma_\mathrm{p} > 0$. The coupling current $\widehat{I}$ produced by an equivalent piezoelectric layer is

$$\widehat{I} = j\omega C_0\widehat{V} - \Gamma_\mathrm{p}\widehat{V}_\mathrm{m} \tag{42}$$

where $C_0 = \epsilon_{33}^{\mathrm{S}}\frac{wL}{t_\mathrm{p}}$ is the equivalent nominal capacitance of the piezoelectric transducer and $\epsilon_{33}^{\mathrm{S}}$ is the permittivity component at constant strain with the plane-stress assumption of a thin narrow beam (i.e. $\epsilon_{33}^{\mathrm{S}} = \epsilon_{33}^{\mathrm{T}} - d_{31,\mathrm{p}}^2/s_{11}^{\mathrm{E}}$). Here, we denote $\widehat{V}_\mathrm{m} = \widehat{V}_2 - \widehat{V}_1$. The complete equivalent circuit is developed as shown in figure 2 where notations of the forces, applied magnetic field and output voltage are in the time domain for a general view.

Under free-free conditions, $\widehat{F}_1 = \widehat{F}_2 = 0$ (which leads to mechanical short-circuit). The lumped-model is then simplified to that depicted in figure 3, where

$$Z = Z_1/2 + Z_2 = \frac{1}{2}\left(\frac{n}{s_{11}^{\mathrm{E}}} + \frac{1-n}{\kappa s_{33}^{\mathrm{H}}}\right)\frac{A}{j\overline{v}}\cot(kL/2). \tag{43}$$

The damping coefficient b (not shown in figure 2) represents the mechanical loss. Additionally, the electrical terminals are now connected to a load resistance R_L. The input equivalent 'force' is defined as $\widehat{F}_0 = \Gamma_\mathrm{m}\widehat{H}_3$ (or $F_0 = \Gamma_\mathrm{m} H_3$ in the time domain). The short-circuit resonance frequency, is determined by the condition $Z = 0$, or equivalently

$$\cos(\frac{\omega L}{2\overline{v}}) = 0, \tag{44}$$

which results in

$$\omega_0 = \pi\frac{\overline{v}}{L}. \tag{45}$$

The resonance frequency depends on the beam length, the thickness ratio, and the material properties, but not on the width of the beam. This property is distinguished from the bending operation of a cantilever beam with a tip mass, in which the bending resonance frequency is a function of the beam width [5].

4. Magnetoelectric coefficient

We now consider the ratio of the electric field E_3 to the external magnetic field H_3. Under open circuit operation (i.e. $R_L \to +\infty$),

$$\widehat{I}_\infty = 0, \tag{46}$$

$$\widehat{V}_\infty = \frac{\Gamma_p}{C_0}\frac{\widehat{V}_m}{j\omega} = \frac{\Gamma_p}{C_0}\widehat{X} = \frac{\Gamma_p}{C_0}\frac{\widehat{F}_0}{j\omega(Z+b)+\dfrac{\Gamma_p^2}{C_0}} \tag{47}$$

Therefore, the ME coefficient is

$$\alpha_{ME} = \left|\frac{d\widehat{E}_{3,\infty}}{d\widehat{H}_3}\right| = \frac{\Gamma_p}{t_p C_0}\frac{\Gamma_m}{\sqrt{(\omega b)^2 + \left(\overline{Z} + \Gamma_p^2/C_0\right)^2}} \tag{48}$$

where $\overline{Z} = j\omega Z$ is a real function of the drive frequency ω, as follows

$$\overline{Z} = \frac{1}{2}\left(\frac{n}{s_{11}^E} + \frac{1-n}{\kappa s_{33}^H}\right)\frac{A}{\overline{v}}\omega\cot\left(\frac{\omega L}{2\overline{v}}\right). \tag{49}$$

The anti-resonance frequency (i.e. the open-circuit resonance frequency), denoted by ω_1, is determined by

$$\overline{Z} + \Delta K = 0 \tag{50}$$

where $\Delta K = \Gamma_p^2/C_0$. Equation (50) has a general form of $X\cot(X) = C$ where X is a variable and C is a constant. There does not exist any analytical solution for this problem, hence, using a numerical method is more suitable. At $\omega = \omega_1$, the ME coefficient is reduced to

$$\alpha_{ME,1} = \frac{\Gamma_p\Gamma_m}{t_p C_0 \omega_1 b}. \tag{51}$$

For moderate electromechanical coupling of the piezoelectric phase $\omega_1 \approx \omega_0$, so $\alpha_{ME,1}$ is approximately $\Gamma_p\Gamma_m/(t_p C_0 \omega_0 b)$. In principle, $\alpha_{ME,1}$ is the maximum possible ME coefficient that can be obtained for a given ME transducer. The compact form in (51) is maybe the most convenient means to evaluate the performance of a ME composite from a material perspective (in other words, from an application-independent point of view).

5. Power optimization

5.1. Analytical solution of output power

We now utilize the equivalent circuit model developed in section 3 to investigate the transferred power in terms of the load resistance, the drive frequency, and the applied **B**−field. The complex amplitude of the output voltage is derived as

$$\widehat{V} = \frac{\Gamma_p}{C_0}\frac{j\omega R_L C_0}{1+j\omega R_L C_0}\widehat{X} = \frac{\Gamma_p}{C_0}\frac{j\omega\tau}{1+j\omega\tau}\widehat{X} \tag{52}$$

where the electrical time constant is $\tau = R_L C_0$. The complex displacement amplitude is

$$\widehat{X} = \frac{\widehat{V}_m}{j\omega} = \frac{\widehat{F}_0}{j\omega(Z+b) + \dfrac{\Gamma_p^2}{C_0}\dfrac{j\omega\tau}{1+j\omega\tau}}. \tag{53}$$

Assuming that, in the time domain, the applied magnetic field has the form of $H_3 = H_0\cos(\omega t)$, the average output power is obtained as

$$P = \frac{1}{2}\frac{\left|\widehat{V}\right|^2}{R_L} = \frac{1}{2}\Delta K\frac{\omega^2\tau}{1+(\omega\tau)^2}\left|\widehat{X}\right|^2 \tag{54}$$

where the square of the displacement amplitude in the frequency domain is given by

$$\left|\widehat{X}\right|^2 = \frac{(\Gamma_m H_0)^2}{\left[\overline{Z} + \Delta K\dfrac{(\omega\tau)^2}{1+(\omega\tau)^2}\right]^2 + \left[\omega b + \Delta K\dfrac{\omega\tau}{1+(\omega\tau)^2}\right]^2}. \tag{55}$$

From (54) and (55), we observe that the power delivered to the load is proportional to the square of both the magnetic field strength and the magneto-elastic transduction factor. For a given external magnetic field, magnetostrictive materials with higher $d_{33,m}$ are preferable as they provide stronger Γ_m, and as a consequence, higher output power.

5.2. Optimum power at resonance and anti-resonance frequencies

Typically, optimal operating frequencies of a resonant generator, such as piezoelectric energy harvesters [5], are close to either the resonance or anti-resonance frequency. Therefore, the maximum output power of the ME WPTS can also be estimated by considering the system performance at these specific frequencies.

At the resonance frequency $\omega = \omega_0$ and $\overline{Z} = 0$. By using the gradient descent method, the optimal load and the corresponding optimum output power are determined as follows:

$${}^{opt}R_L|_{\omega=\omega_0} = \frac{1}{\omega_0 C_0\sqrt{M_0^2+1}}, \tag{56}$$

$$P_0 = {}^{opt}P|_{\omega=\omega_0} = \frac{(\Gamma_m H_0)^2}{4b}M_0\left(\sqrt{M_0^2+1} - M_0\right). \tag{57}$$

M_f is a resonator figure of merit, defined as $M_\mathrm{f} = \Delta K/(b\omega)$. In particular, at the resonance frequency $M_0 = \Delta K/(b\omega_0)$. We can write $M_0 = k_\mathrm{e}^2 Q_{0,\mathrm{p}}$ where k_e is the expedient coupling coefficient (or the generalized electromechanical coupling coefficient) and $Q_{0,\mathrm{p}}$ is the mechanical quality factor of the piezoelectric phase at the resonance frequency ω_0. The details of the derivation are presented in appendix B. A high figure-of-merit is achieved when a piezoelectric material shows strong electromechanical coupling and low mechanical losses, simultaneously. With the same applied magnetic field, based on (41), we can infer the following properties, increasing the amount of the magnetostrictive material or the ratio of the piezomagnetic coefficient to the compliance constant $(d_{33,\mathrm{m}}/s_{33}^\mathrm{H})$, results in higher output power.

In the same manner, at the anti-resonance frequency $\omega = \omega_1$ (and thus $\overline{Z} = -\Delta K$), we get

$$ {}^{\mathrm{opt}}R_\mathrm{L}|_{\omega=\omega_1} = \frac{\sqrt{M_1^2+1}}{\omega_1 C_0}, \tag{58} $$

$$ P_1 = {}^{\mathrm{opt}}P|_{\omega=\omega_1} = \frac{(\Gamma_\mathrm{m} H_0)^2}{4b} M_1\left(\sqrt{M_1^2+1} - M_1\right) \tag{59} $$

where $M_1 = \Delta K/(b\omega_1)$. In general, P_0 and P_1 are not identical, however for moderately coupled systems $M_0 \approx M_1$, the two maximum powers approximately coincide $P_0 \approx P_1$. It should be noted that the inequality $M_\mathrm{i}(\sqrt{M_\mathrm{i}^2+1} - M_\mathrm{i}) < 1/2$ always holds true for all $M_\mathrm{i} > 0$ ($\mathrm{i} \in \{1,2\}$), therefore P_0 and P_1 are less than $P_\mathrm{avt} = (\Gamma_\mathrm{m} H_0)^2/(8b)$ which is the maximum power available for transfer [5]. As M_0 and M_1 increase, the two ratios P_0/P_avt and P_1/P_avt approach unity.

6. Model validations

6.1. Experimental setup

Figure 4 shows the experimental setup used for validating the equivalent two-port model. The Helmholtz coil is a transmitter that produces a uniform magnetic flux density as a means of power transfer. The receiver is a magnetoelectric laminated composite, consisting of two TdVib Galfenol and one PZT-5A layers. The magnetostrictive and piezoelectric phases are bonded together by a conductive epoxy, EPO-TEK H20S. Four permanent magnets placed on top, bottom, and two sides (not shown in the figure) of the ME transducer provide a DC bias field for its operation. The two Galfenol layers are magnetized in the length axis; meanwhile, the PZT-5A layer is poled in the thickness direction. The Helmholtz coil is controlled by a Tektronix function generator connecting to an E&I 210 L RF power amplifier. The induced voltage across the load resistance is measured and collected by a Tektronix oscilloscope. The average output power is then computed as $P = \frac{1}{T}\int_0^T \frac{V^2(t)}{R_\mathrm{L}}\mathrm{d}t$. The geometry of the ME generator, the Helmholtz coil, and the material properties are listed in table 1, except the interface coupling coefficient κ and the longitudinal piezomagnetic constant $d_{33,\mathrm{m}}$, which are determined by fitting to experiments in the next Sections.

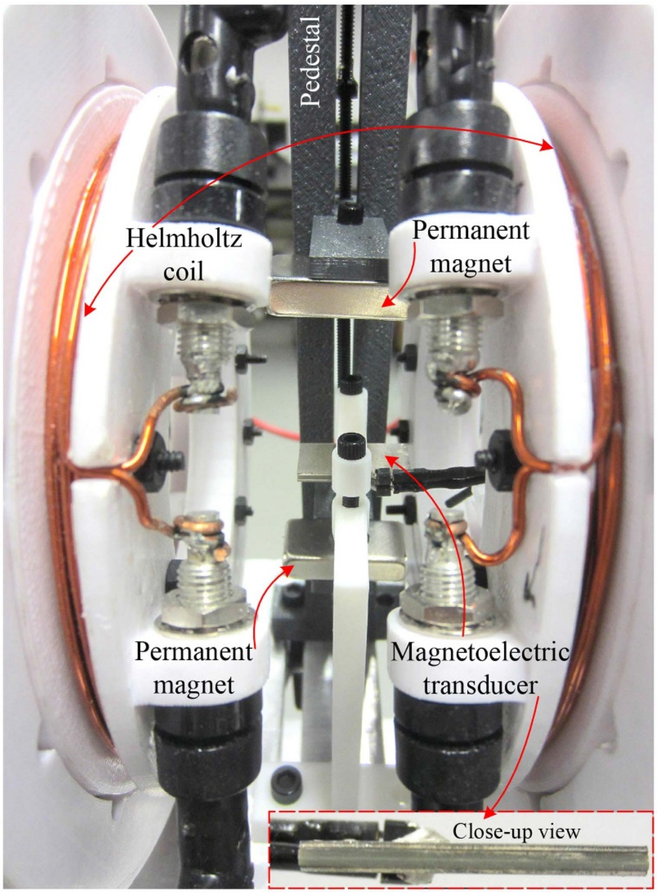

Figure 4. Experimental setup, in which a circular Helmholtz coil is used as a transmitter, the magnetoelectric transducer is placed at the center of the coil, and four permanent magnets are utilized as DC field bias.

6.2. Parameter identifications

Since the piezomagnetic coefficient $d_{33,\mathrm{m}}$ is a function of the DC bias field, the possible optimal value of $d_{33,\mathrm{m}}$ can be obtained by manually adjusting the distances between the permanent magnets and the ME laminated composite. The DC field that yields the maximum open-circuit voltage generated by the ME transducer is considered as optimal. Here, the bias field is read by the DC Gaussmeter Model GM1-ST (AlphaLab, Inc.), and the open-circuit output voltage is approximately measured with Tektronix 10 MΩ probes. By varying the drive frequency, the anti-resonance frequency, at which the open-circuit voltage reaches its maximum, is determined. The optimal DC bias field and the corresponding anti-resonance frequency are $\sim$13.31 mT and $f_1 \approx 70.47$ kHz respectively. The interface coupling coefficient κ is then estimated by fitting the solution ω_1 of equations (49) and (50) to the experimental value, which results in $\kappa = 62.2\,\%$.

We note that, the output voltage is proportional to the displacement of the laminated composite. Considering a damped harmonic oscillation of the open-circuit voltage shown in figure 5, the damping ratio ξ can be extracted with an exponential fit through the local maxima of this underdamped response ($\xi < 1$). The least-squares method is formulated as follows

Table 1. Material properties and device geometries.

Parameters	Value
PZT-5A4E	
Elastic constant, Y_{11}^{E}	66, GPa
Elastic compliance, s_{11}^{E}	$1/Y_{11}^{\mathrm{E}}$, $\mathrm{m^2/N}$
Piezoelectric constant, $d_{31,\mathrm{p}}$	-190×10^{-12}, m/V
Dielectric permittivity, $\epsilon_{33}^{\mathrm{T}}/\epsilon_0$	1800
Mass density, ρ_{p}	7800 kg/ $\mathrm{m^{-3}}$
TdVib Galfenol	
Elastic constant, Y_{33}^{H}	40, GPa
Elastic compliance, s_{33}^{H}	$1/Y_{33}^{\mathrm{H}}$, $\mathrm{m^2/N}$
Magnetic permeability, $\mu_{33,\mathrm{m}}^{\mathrm{T}}/\mu_0$	100
Mass density, ρ_{m}	7800 kg/ $\mathrm{m^{-3}}$
ME transducer geometry	
PZT thickness, t_{p}	1.02, mm
Galfenol thickness (each layer), t_{m}	370, μm
Total thickness, $t_0=t_{\mathrm{p}}+2t_{\mathrm{m}}$	1.76, mm
Laminated composite width, w	10, mm
Laminated composite length, L	20, mm
Helmholtz coil geometry	
Diameter (center of cross-section)	91, mm
Nominal cross-section	49×49, $\mathrm{mm^2}$
Wire gauge	16
Number of turns	9

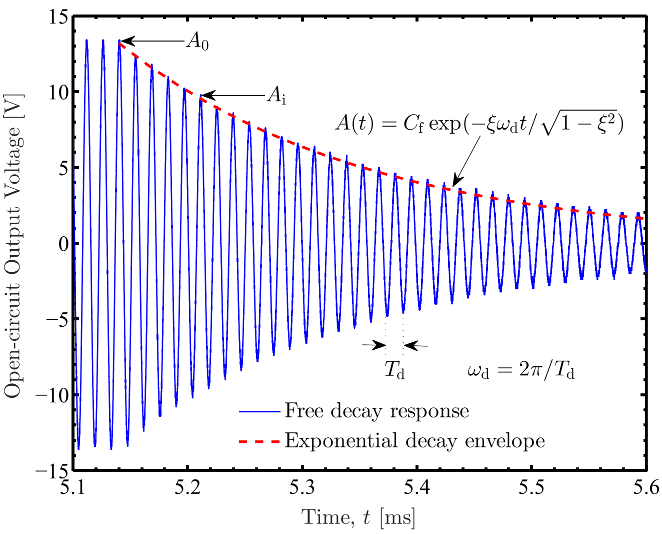

Figure 5. A comparison of (i) free decay response of the open-circuit output voltage, and (ii) exponential decay envelope through local maxima A_{i}, where $\mathrm{i}\in\mathbb{N}$. A_0 is the highest maximum and $C_{\mathrm{f}}=2.12\times10^{11}$ is a fitted constant.

$$\min_{\xi>0,\,C_{\mathrm{f}}>0}\sum_{\mathrm{i}=0}^{N}\left[A(t_{\mathrm{i}})-A_{\mathrm{i}}(t_{\mathrm{i}})\right]^2 \tag{60}$$

where $(N+1)$ is the number of experimental samples collected. The decay envelope is characterized by the exponential function $A(t)=C_{\mathrm{f}}\exp\left(-\xi\omega_{\mathrm{d}}t/\sqrt{1-\xi^2}\right)$ where C_{f} is an unknown constant. The angular damped resonance frequency is calculated as $\omega_{\mathrm{d}}=2\pi/T_{\mathrm{d}}$, where T_{d} is the damped period. The discrete oscillation maxima, denoted as A_{i} ($\mathrm{i}\in\mathbb{N}$), with their corresponding time of occurrence t_{i}, are obtained from the decaying waveform. To solve this non-linear problem with inequality constraints, the non-linear Interior Point and Sequential Quadratic Programming approaches can be used [42]. The fitting procedure gives $\xi\approx10.68\times10^{-3}$; accordingly, the mechanical quality factor around the resonance is $Q_{\mathrm{m}}\approx46.81$.

For a mass-spring-damper system, the damping ratio is defined as $\xi=b/(2\sqrt{mK_0})$ where b is the damping coefficient which represents total mechanical losses, K_0 is the short-circuit stiffness and m is the mass. However, the mechanical impedance Z of the ME generator is an indispensable function of the material properties and the geometry. Therefore, in order to evaluate the damping constant, we approximate Z by an equivalent mass-spring model, where K_0 and m are found by the least-squares optimization scheme

$$\min_{K_0>0,\,m>0}\sum\left[\left(\omega m-\frac{K_0}{\omega}\right)-|Z|\right]^2 \tag{61}$$

where the angular drive frequency ω is chosen in a range around the resonance frequency ω_0. The numerical minimization yields the following results, $K_0=81.48$ MN $\mathrm{m^{-1}}$ and $m=445.8$ mg, which leads to $b=4.22$ Ns $\mathrm{m^{-1}}$.

From (47) and (50), the open-circuit voltage amplitude at the anti-resonance frequency is derived as

$$V_{\infty,1}=\Gamma_{\mathrm{m}}\frac{H_0\Gamma_{\mathrm{p}}}{C_0\omega_1 b} \tag{62}$$

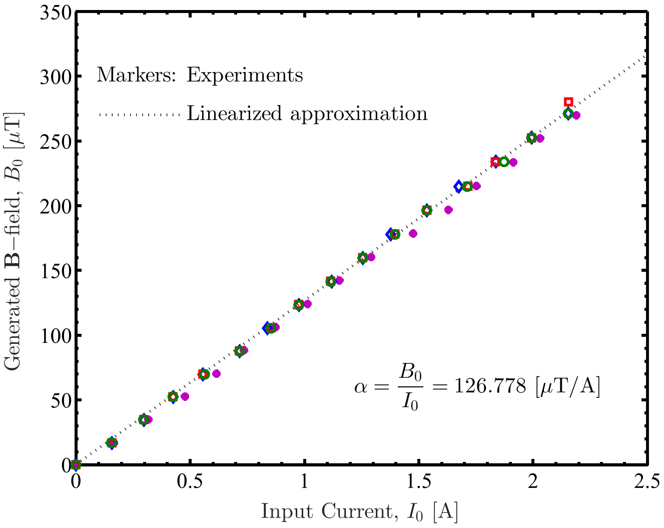

Figure 6. Characterization of the **B**−field generated at the center of the Helmholtz coil, with respect to the current input to the coil. B_0 and I_0 are the amplitude values.

where Γ_m is a function of $d_{33,m}$. The piezomagnetic constant $d_{33,m}$ is approximated by fitting the model prediction in (62) to the measured value, giving us a coefficient of $d_{33,m} = 7.77 \times 10^{-9}$ Wb/N, which is within the range reported by other authors, e.g. 1.85×10^{-9} Wb N^{-1} in [43] and 16.5×10^{-9} Wb N^{-1} in [44]. The measured nominal capacitance of the piezoelectric layer is $C_0 = 2.95$ nF. Up to this point, all the model coefficients are given. This same set of parameters is then used for validating all following cases.

6.3. Experimental validations

(i) Due to the difficulty in measuring the **B**−field while conducting experiments, and (ii) to avoid any possible interference of the permanent magnets (used as the bias field), the relationship between the magnetic flux density strength and the input current is quantified before completing the experimental setup. Four sets of measurements are carried out. The current through the Helmholtz coil and the **B**−field generated at the coil center are captured by the Rigol RP1001C current probe and the AC milliGauss meter model UHS2, respectively. Note, the value displayed on the Gauss meter is in root mean square (RMS) form. The obtained results are shown in figure 6. The relationship between the two parameters is expressed by a linearized approximation, $\alpha = B_0/I_0 = 126.3778\ \mu$T A^{-1}, which is then utilized to map the external **B**−field amplitude from the measured current in further experiments.

Figure 7 presents the frequency response of the open-circuit voltage amplitude with two different ranges of the applied **B**−field. Comparisons between the experimental data and the simulation results (predicted by the equivalent two-port model) show a consistently good agreement for both cases. The output voltage is measured at the steady-state with discrete drive frequencies. It should be noted that the impedance of the Helmholtz coil is dependent on the frequency. Therefore, given the same source voltage, the input current decreases with respect to the increase of the operating frequency, which hence reduces the **B**−field strength. In the simulations, V_∞ is computed as a function of both the drive frequency and its corresponding **B**−field amplitude, $V_\infty = V_\infty(\omega, B_0(\omega))$.

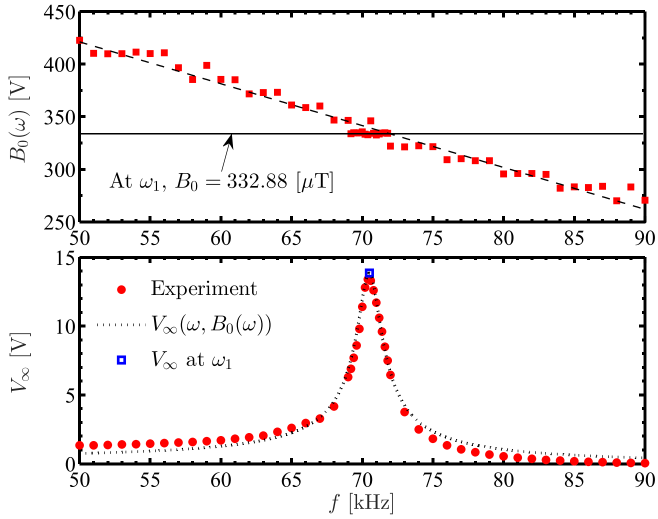

(a) $B_0 \in [422.64 \to 270.06]$ [μT]

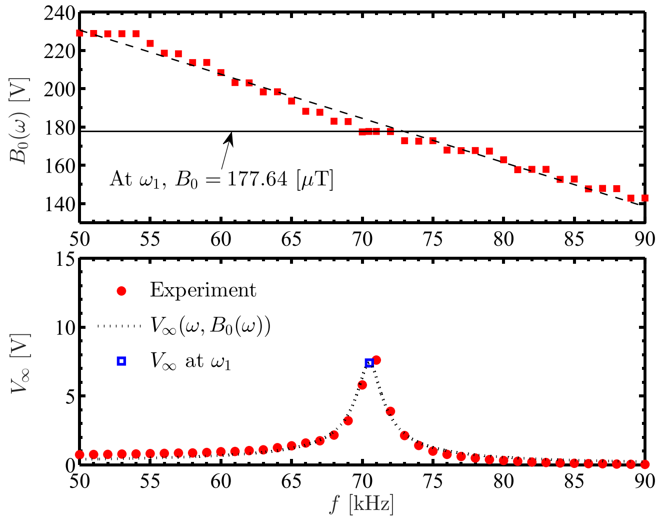

(b) $B_0 \in [229.05 \to 142.85]$ [μT]

Figure 7. Frequency response comparisons between the experimental data and simulation results by the model. V_∞ is the open-circuit output voltage, measured with 10 MΩ probes. $V_{\infty,1}$ (V_∞ at the anti-resonance frequency ω_1) is determined from (62), in which $B_0 = 332.88\ \mu$T and $177.64\ \mu$T are used for the two cases.

Figure 7 also reveals that (50) is the exact equation to solve for the anti-resonance frequency ω_1, and $V_{\infty,1}$ computed by (62) can be used to estimate the maximum possible open-circuit voltage. Since $\alpha_{ME} \propto V_\infty$, this means $\alpha_{ME,1}$ is the highest magnetoelectric coefficient that can be achieved. α_{ME} is widely used as a critical criterion for the magnetoelectric coupling properties in multiferroic materials. However, most of the expressions of α_{ME} reported in the literature concern the operation of a ME device at low-frequency ranges (far below the resonance), which may lead to unfair comparisons among ME transducers (e.g. [45, 46]). Therefore, from

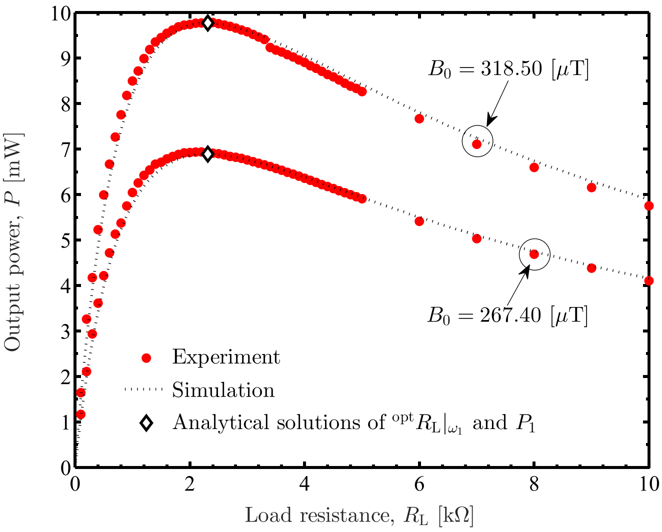

Figure 8. Output power with respect to load resistance with different applied magnetic flux density: Comparisons between experimental data and simulation results. The drive frequency is at the anti-resonance frequency, $f_1 = 70.47$ kHz. The analytical solutions of ${}^{\rm opt}R_{\rm L}|\omega_1$ and P_1 are obtained from (58) and (59), respectively.

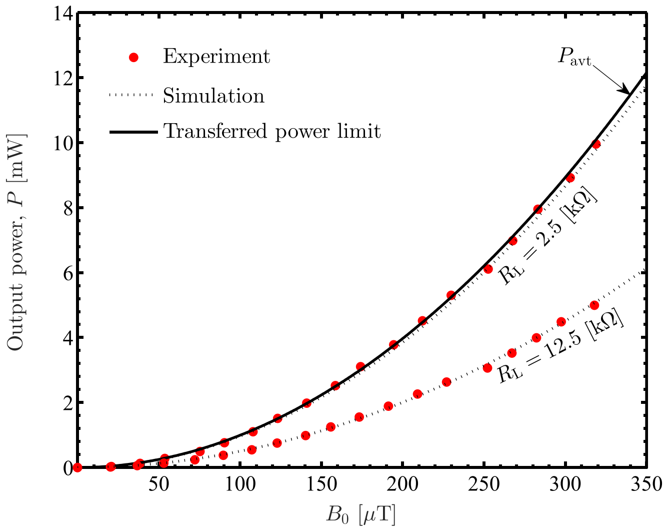

Figure 9. Comparisons of the external **B**−field responses between the model simulations and measured results with the optimal load of ${}^{\rm opt}R_{\rm L}|\omega_1 = 2.5$ kΩ and an arbitrary load of $R_{\rm L} = 12.5$ kΩ. The maximum power available for transfer is $P_{\rm avt} = (\Gamma_{\rm m}H_0)^2/(8b)$.

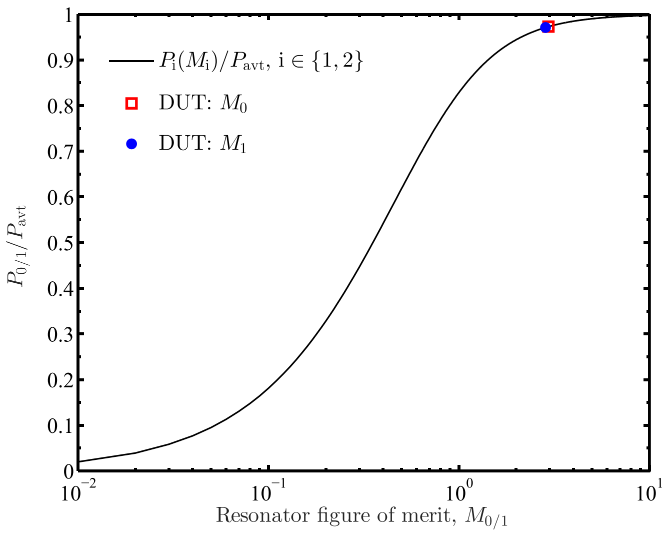

Figure 10. Ratio between the optimum output power attained at the (anti-)resonance frequency $P_{0/1}$ and the power limit $P_{\rm avs}$ as functions of the resonator figure of merit $M_{0,1}$, computed by (57) and (59). The particular values of $M_{0,1}$ and their corresponding power ratios of the investigated ME transducer are included. Notation: DUT = Device Under Test.

the material point of view, $\alpha_{\rm ME,1}$ is perhaps a more appropriate and efficient alternative means to theoretically evaluate the performance of a ME-based system. Although $\alpha_{\rm ME}$ is not the main objective of this work, its corresponding frequency response is presented in appendix A.

Figure 8 shows the variation of the output power with respect to the load resistance for two **B**−field amplitudes. The drive frequency is set at the anti-resonance frequency, $f_1 = \omega_1/(2\pi) = 70.47$ kHz, for all measurements. The difference between experiments and simulations is negligible. A maximum transferred power of $\max\{{\rm P}\} = 9.78$ mW is achieved at $B_0 = 318.50$ μT, with an optimal load of ${}^{\rm opt}R_{\rm L} \in [2.1, 2.5]$ kΩ (note that any value of $R_{\rm L}$ in this resistance range produces almost the same output power). The corresponding analytical solutions derived from the model are $P_1 = 9.77$ mW and ${}^{\rm opt}R_{\rm L}|\omega_1 = 2.3$ kΩ, attained from (58) and (59), respectively. The model accuracy is consistent with $B_0 = 267.40$ μT. As expected, (i) The optimum electrical load is independent of B_0, and (ii) Higher input magnetic field strength results in stronger interaction acting on the Galfenol layers, and as a consequence, higher power delivered to the load.

Figure 9 presents the variation of the output power P with respect to the external magnetic flux density B_0. The drive frequency is fixed at f_1. The experimental and theoretical results are in good agreement in both cases, with the optimal load of ${}^{\rm opt}R_{\rm L}|\omega_1 = 2.5$ kΩ and with an arbitrary load of $R_{\rm L} = 12.5$ kΩ. As predicted by the theory, P is a quadratic function of B_0. The optimum power delivered to the load at the anti-resonance frequency P_1 and the power limit $P_{\rm avt}$ are very close to each other. This observation can be explained by figure 10. It shows the ratio of $P_{0/1}$ to the power bound, $P_{\rm avt}$, as a function of the resonator figure of merit $M_{0/1}$. For the device under consideration, $M_0 = 2.95$ and $M_1 = 2.85$, which leads to $P_0/P_{\rm avt} \approx P_1/P_{\rm avt} \approx 97\%$. In general, $M_{0/1} \approx 2$ or higher is a sufficient condition such that $P_{0/1}$ approaches its physical limit $P_{\rm avt}$. From practical point of view, determining and operating the ME transducer at its anti-resonance frequency along with the corresponding optimal load is perhaps the most convenient technique to approach the power limit.

For the system in use, the overall efficiency is relatively low, $\eta \approx 0.12\%$. The details of this experimental study are presented in appendix C, in order to keep the article focused on the power delivered to the load at a given incident magnetic field, regardless of how the field is produced or the power required to generate it. The question on how to improve the transfer efficiency is out of the scope of this work and is open for further investigation.

Despite the apparent complexity of the multi-domain energy conversion property of the ME WPTS, the equivalent circuit model has been consistently accurate in predicting all of the essential behaviors related to frequency, load, and magnetic field responses. The developed model is reliable in capturing both of the ME coefficient and the actual power transferred to the load.

The simulation results obtained from the model reveal the following characteristics. When the length of the composite changes (half or double, for instance), only the corresponding optimal load is adjusted, the power available for transfer P_{avt}, and the maximum output power $P_{0/1}$ are kept the same, given an applied magnetic field strength. An advantage of the longer beam is that its resonance and anti-resonance frequencies are lower, which allows higher permissible external magnetic flux density, and thus results in higher transferred power. Meanwhile, a shorter beam achieves higher power density, with identical incident **B**–field. The increase of the width allows the laminate to capture more magnetic flux (i.e. inducing higher Γ_{m}), which enhances both P_{avt} and $P_{0/1}$. Similar effects are observed when increasing the Galfenol thickness. However, further increasing the thickness of PZT does not give a significant benefit as the current thickness can already approach the physical power limit. In a general trend, decrease of t_{m} and t_{p} leads to smaller Γ_{m} and Γ_{p}, respectively, and drop of $P_{0/1}$. In the circumstance where the total thickness t_0 is constrained, there exists an optimal ratio of t_{p} to t_0, $n = t_{\mathrm{p}}/t_0$; for the material properties shown in this article, the optimum value is $n_{\mathrm{opt}} = 0.14$ with the maximum output power of $P_{0/1} = 33.72$ mW at $B_0 = 318.5\ \mu$T. The effects of the material constants, such as $d_{31,\mathrm{p}}$ and $d_{33,\mathrm{m}}$, are discussed in the next section.

7. Discussions

The ME coefficient α_{ME} has been widely used as a standard to evaluate the performance of ME-based devices; the higher α_{ME}, the stronger the ME effect, and the better the quality of the ME materials. However, is it true that higher α_{ME} always gives better output power? The main aim of this section is to seek the answer to that question, based on the equivalent circuit model validated in the previous section.

The electrodynamic and electromechanical transduction factors, Γ_{m} and Γ_{p}, represent the energy transfer mechanisms between the magnetic-mechanical-electrical domains. Considering the analytical solutions for the optimum ME coefficient and output power in (51) and (59), we observe that both $\alpha_{\mathrm{ME},1}$ and P_1 are functions of Γ_{m} and Γ_{p}. The behavior of $\alpha_{\mathrm{ME},1}$ and P_1 in terms of Γ_{m} are shown in figure 11, where Γ_{m} is treated as a variable and the other model parameters, such as Γ_{p}, C_0, ω_1 and b, are kept unchanged. In a general trend, $\alpha_{\mathrm{ME},1}$ and P_1 always increase with the increase of Γ_{m}. However, while $\alpha_{\mathrm{ME},1}$ is linearly proportional to Γ_{m}, P_1 is a quadratic function of Γ_{m}. It is essential to note that higher

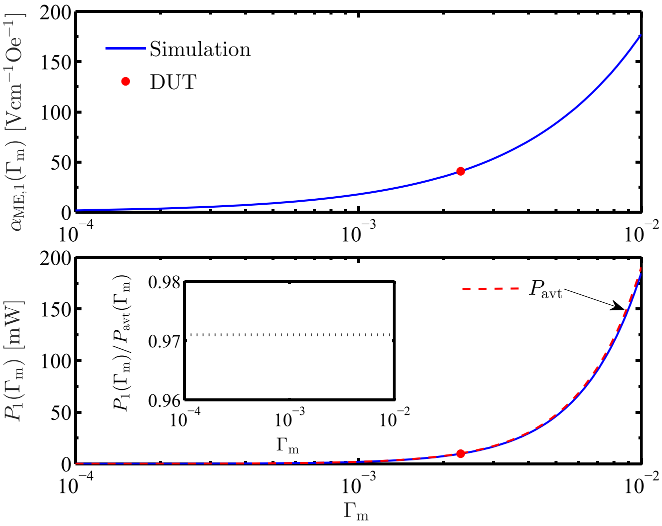

Figure 11. Optimum output power and ME coefficient, P_1 and $\alpha_{\mathrm{ME},1}$, with respect to the electrodynamic transduction factor Γ_{m}. The ratio of P_1 to P_{avt}, and the measured results of the DUT are also included for comparisons.

Γ_{m} leads to higher power available for transfer, given a constant applied **B**−field. Nonetheless, the discrepancy between P_1 and P_{avt} is negligible. The ratio of P_1 to P_{avt} is close to unity for all Γ_{m} as depicted in the sub-figure; in particular, $P_1/P_{\mathrm{avt}} = 97.1\%$. At $\Gamma_{\mathrm{m}}^* = 10^{-2}$, which is 4.35 times of that of the DUT, the maximum output power reaches $P_1^* = 190.3$ mW. In practice, this can be achieved with the use of other magnetostrictive materials instead of Galfenol. Among those, Metglas and FeGaB thin film are two promising alternatives, as their piezomagnetic coefficients, $d_{33,\mathrm{m}}$, are much higher than that of Galfenol (denoted as G) [34], and therefore result in higher Γ_{m}. For example, the piezomagnetic coefficient and elastic compliance of Metglas (M) are $d_{33,\mathrm{m}}(\mathrm{M}) = 50.3 \times 10^{-9}$ m A^{-1} and $s_{33}^{\mathrm{H}}(\mathrm{M}) = 40 \times 10^{-12}$ m^2 N^{-1} [34], and the ratio between the two electrodynamic transduction factors is $\Gamma_{\mathrm{m}}(\mathrm{M})/\Gamma_{\mathrm{m}}(\mathrm{G}) = 4.05$, given the same geometry. From the efficiency perspective, P_1^* is still far below the input power, which is approximately 8.2 W. Thus, there remains considerable room for the improvement of η associated with material development.

By definition, the longitudinal piezomagnetic coefficient is the rate of change of the magnetostrictive strain along the axial direction ε with respect to the DC bias magnetic field H_{b}. In particular, $d_{33,\mathrm{m}} = \mathrm{d}\varepsilon(M)/\mathrm{d}H_{\mathrm{b}}$ where M is the magnetization and is induced by H_{b} [47]. Both ε and $d_{33,\mathrm{m}}$ are zero before the magnetostrictive material is magnetized. ε increases with M and then reaches its saturation value when the magnetization is saturated. Due to this behavior of ε, initially, $d_{33,\mathrm{m}}$ increases. However, there exists a certain strength of H_{b} at which $d_{33,\mathrm{m}}$ attains a maximum. Beyond that point, $d_{33,\mathrm{m}}$ decreases. Since the physical limitations of $d_{33,\mathrm{m}}$, and thus Γ_{m}, are determined by the magnetic properties of the material, the power available for transfer P_{avt} cannot increase infinitely for a given **B**−field. Furthermore, P_{avt} is rigorously constrained by the power input to the transmitter coil P_{i}. However, with the range of Γ_{m} shown

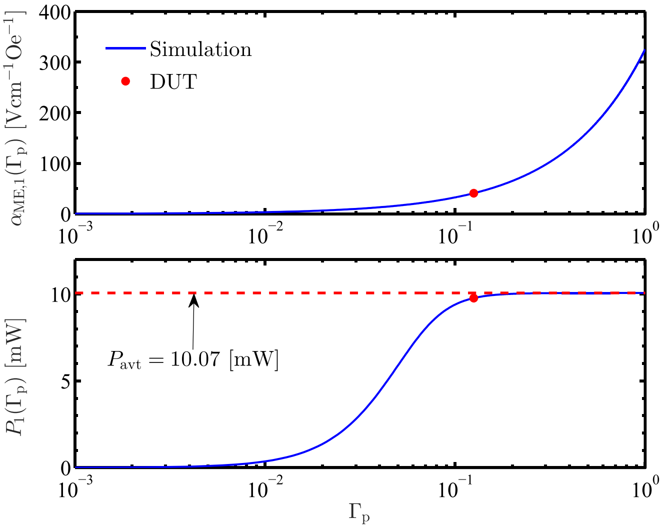

Figure 12. Variations of the optimum output power and ME coefficient, P_1 and $\alpha_{\mathrm{ME},1}$, with respect to the electromechanical transduction factor Γ_p. The measured results of the DUT are also included for comparisons. P_avt is a constant.

in figure 11, $P_1 \approx P_\mathrm{avt} \ll P_\mathrm{i}$, therefore, the limit of P_avt is not seen.

In the same manner, the influence of Γ_p on the performance of $\alpha_{\mathrm{ME},1}$ and P_1 is presented in figure 12. The roles of Γ_m and Γ_p are now switched and Γ_p becomes a variable. Similarly, $\alpha_{\mathrm{ME},1}$ is a linear function of Γ_p. However, P_1 saturates to P_avt when Γ_p is large enough. In this case, Γ_m is a constant, and hence P_avt is unchanged with respect to Γ_p. Moreover, with the use of PZT-5A4E as in the experiments, we get $P_1 \approx P_\mathrm{avt}$. Alternating PZT-5A4E by another piezoelectric material that has higher $d_{31,\mathrm{p}}$, and therefore higher Γ_p, does not make any significant improvement on the output power as it nearly approaches its physical limit. This finding demonstrates that an increase in the ME coefficient does not ensure increased power delivered to the load. Only considering α_ME as a critical criterion to anticipate the performance of a ME WPTS may be not appropriate. Instead, separately assessing the role of each phase, magnetostrictive and piezoelectric, is a more comprehensive view. While Γ_m defines the physical bound of the power that can be transferred to the load, Γ_p (as an alternative to the figure of merits $M_{0/1}$) indicates whether the device is able to reach that limit or not. Note that, when the mechanical damping coefficient b decreases, the required value of Γ_p, at which $M_1 \approx 2$ and P_1 starts to saturate, also decreases due to the relationship $M_1 = \Gamma_\mathrm{p}^2/(b\omega_1 C_0)$. We hope this recommendation is able to clarify possible misunderstandings in the literature, and have an impact on the design considerations of a ME WPTS.

8. Conclusions

We have presented a comprehensive mathematical modeling framework and analytical solutions to the power optimization problem for a WPTS utilizing a ME transducer as a receiver. An equivalent two-port model was derived and validated by different sets of rigorous experiments. Several techniques for identifying unknown parameters were discussed. The model developed was able to sufficiently capture and predict the behavior of the device with respect to the drive frequency, load resistance, and applied magnetic flux density, despite the apparent sophisticated-dynamics of a multiple-domain system. We especially emphasized the essential role of the electrodynamic (also known as magneto-elastic) transduction factor in determining the maximum possible power generated at the load with a constant external B-field. We simultaneously showed that this power bound can be approached if the two following conditions are satisfied. (i) The ME generator is operating at the anti-resonance frequency, and the electrical load is optimized correspondingly. (ii) The electromechanical transduction factor reaches a particular range. These alternative criteria (for both transduction mechanisms) are more appropriate for evaluating the performance of a ME WPTS than the ME coefficient that has been widely utilized in the literature.

Acknowledgment

This work was supported by the National Science Foundation ASSIST Nanosystems ERC under Award Number EEC-1160483.

Appendix A. Frequency response of the magnetoelectric coefficient α_ME

Figure A1 shows the frequency response of the ME coefficient α_ME with the unit of Vcm^{-1}Oe^{-1} that is the most common use in the material science community. The simulation results are calculated from (48) and the measured data are given by $(V_\infty/t_\mathrm{p})/H_0$, which are in good agreement. The analytical solution of the ME constant at the anti-resonance frequency, $\alpha_{\mathrm{ME},1}$, is able to predict exactly the maximum attainable of α_ME for a given ME transducer. The consistency of the equivalent circuit model is demonstrated by two sets of experiments with different ranges of the applied $\mathbf{B}-$field. As shown in figure 7, these two intervals are dependent on the drive frequency and the initial values of B_0 (or in other words, the power input to the Helmholtz coil). The optimum ME coefficient of the device under test is $\max\{\alpha_\mathrm{ME}\} \approx 40.8$ Vcm^{-1}Oe^{-1}.

Appendix B. Resonator figure-of-Merit

At the resonance frequency ω_0, the figure of merit M_f of the piezoelectric generator is given by

$$M_0 = \frac{\Delta K}{\omega_0 b} = \frac{\Gamma_\mathrm{p}^2}{C_0}\frac{1}{\omega_0 b} = k_\mathrm{e}^2\left(\frac{wt_\mathrm{p}}{s_{11}^\mathrm{E}\pi\overline{v}}\right)\frac{1}{b} \tag{B1}$$

where Γ_p, C_0 and ω_0 are taken from (40), (42) and (45), respectively, and the squared expedient electromechanical

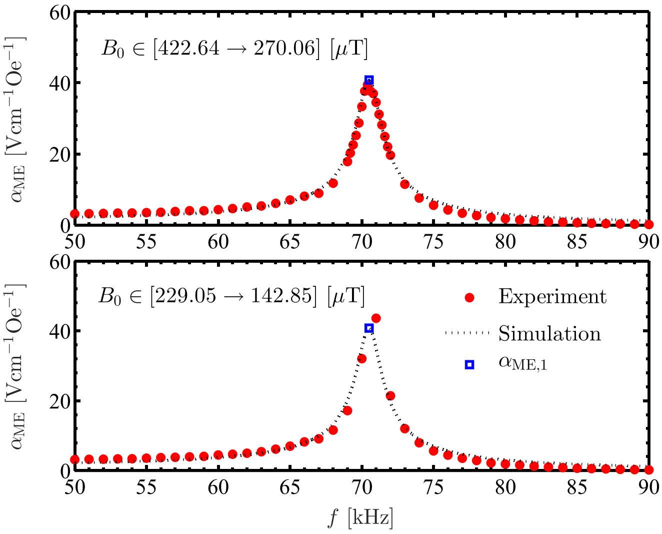

Figure A1. Frequency response of the ME coefficient: Comparisons between the experimental data and simulation results. $\alpha_{\mathrm{ME},1}$ (α_{ME} at ω_1) is achieved from (51). Unit conversion of magnetic field: 1 A/m $= 4\pi \times 10^{-3}$ Oe.

coupling coefficient is

$$k_\mathrm{e}^2 = \frac{d_{31,\mathrm{p}}^2}{s_{11}^\mathrm{E}\epsilon_{33}^\mathrm{S}}. \tag{B2}$$

Introducing an effective compliance s_e, which is determined by

$$\frac{1}{s_\mathrm{e}} = \frac{n}{s_{11}^\mathrm{D}} + \frac{1-n}{\kappa s_{33}^\mathrm{B}}, \tag{B3}$$

we can write

$$\overline{v}^2 = (\overline{\rho} s_\mathrm{e})^{-1}. \tag{B4}$$

The effective mass of the piezoelectric layer can then be defined as

$$m_{\mathrm{e,p}} = \left(\frac{s_\mathrm{e}}{\pi^2 s_{11}^\mathrm{E}}\right)(wt_\mathrm{p}L)\overline{\rho} = \frac{wt_\mathrm{p}L}{s_{11}^\mathrm{E}(\pi\overline{v})^2}. \tag{B5}$$

The mechanical quality factor of the piezoelectric resonator at ω_0 is derived as follows

$$Q_{0,\mathrm{p}} = \frac{m_{\mathrm{e,p}}\omega_0}{b} = \frac{1}{b}\frac{wt_\mathrm{p}L}{s_{11}^\mathrm{E}(\pi\overline{v})^2}\frac{\pi\overline{v}}{L} = \frac{1}{b}\frac{wt_\mathrm{p}}{s_{11}^\mathrm{E}\pi\overline{v}}. \tag{B6}$$

From (B1) and (B6), we get

$$M_0 = k_\mathrm{e}^2 Q_{0,\mathrm{p}}. \tag{B7}$$

Besides k_e^2, M_0 is widely used as an alternative to distinguishing the low- and high-coupling regime.

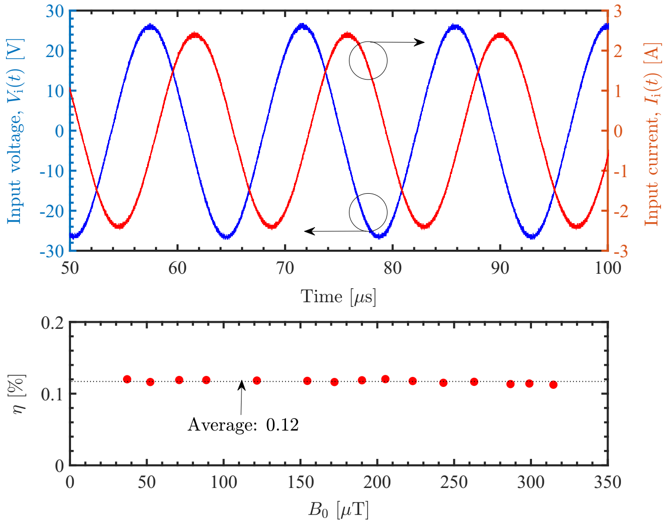

Figure C2. Top: Waveforms of the voltage and current input to the Helmholtz coil that producing a magnetic flux density amplitude of $B_0 = 314.62$ μT. Bottom: Efficiency of the ME WPTS, measured with different values of input power (and therefore generated **B**−field).

Appendix C. An experimental study on transfer efficiency

For low-power applications such as implantable medical devices and wireless sensor networks, the efficiency is often not the central objective. Instead, the ultimate goal is to maximize the power delivered to the load. However, it is still of interest to investigate the transmission efficiency of the ME WPTS.

Figure C2 shows an example of the input voltage and current waveforms that generate a corresponding **B**−field amplitude of $B_0 = 314.62$ μT. The average input power is numerically calculated as

$$P_\mathrm{i} = \frac{1}{t_2 - t_1}\int_{t_1}^{t_2} p_\mathrm{i}(t)\mathrm{d}t \tag{B8}$$

where $[t_1, t_2]$ is the measured time interval, and $p_\mathrm{i}(t)$ is the instantaneous power, $p_\mathrm{i}(t) = V_\mathrm{i}(t)I_\mathrm{i}(t)$. The system efficiency is then determined by the ratio between the power induced on the load and the power input to the network,

$$\eta = \frac{P}{P_\mathrm{i}}. \tag{B9}$$

The measurement is repeated with various values of P_i (which results in an alteration of the input **B**−field strengths accordingly). As seen in the same figure, η is independent of B_0 since both of P_i and P are proportional to B_0^2. The average efficiency of the device under test is $\eta \approx 0.12$ %, which is relatively lower than that of an inductively coupled wireless power transfer device [48–50], though, is comparable to an acoustic or RF energy transmission system [12]. However, the power transfer efficiency of the inductive coupling WPTS drops dramatically as the dimensions of the receiver scale down to mm or μm ranges [51]. Details of a brief quantitative comparison are

Table C1. Comparison of several WPT systems with different transferring mechanisms.

Article	Method	Frequency	Receiver size	Distance	Efficiency
[51], 2016	RIC	200 MHz	1 mm (diameter)	12 mm	0.56 %
[52], 2011	RIC	8 MHz	10×10 mm^2	10 mm	54.98 %
[53], 2010	RF	1 GHz	2×2 mm^2	40 mm	0.2 %
[54], 2014	RF	1.6 GHz	2 mm (diameter)	50 mm	0.04 %
[55], 2014	Acoustic	1 MHz	5×10 mm^2	105 mm	1.6 %
[56], 2019	Acoustic	88 kHz	2×2 mm^2	20 mm	0.33 %
[4], 2018	MME	350 Hz	71.28 mm^3	–	2.5×10^{-3} %
[6], 2019	ED	514 Hz	3 cm^3	10 mm	7 %
This work, 2019	ME	70.47 kHz	352 mm^3	–	0.12 %

presented in table C1. Here, we are not trying to cover all the WPT-related work reported in the literature. Instead, we only choose the latest and the most relevant papers focusing on bio-medical applications as representatives.

For a given operating frequency, an efficient ME receiver can be a few orders of magnitude smaller than that of inductive coupling and RF WPT systems [15]. This advantage of the ME transducer makes it promising for miniaturization, especially for implantable medical devices. Furthermore, it is important to note that the Helmholtz coil is not tuned to the mechanical (anti-)resonance of the ME laminated composite. This means the transmitter is subject to more electrical loss during transfer, thus reducing the overall efficiency. The question of how to improve η is open for further analysis in future work.

ORCID iD

Binh Duc Truong https://orcid.org/0000-0001-7108-4713

References

[1] Int. Commission on Non-Ionizing Radiation Protection 1998 Guidelines for limiting exposure to time-varying electric, magnetic and electromagnetic fields (up to 300 ghz) *Health Phys.* **75** 494–522

[2] Int. Commission on Non-Ionizing Radiation Protection 2010 Guidelines for limiting exposure to time-varying electric and magnetic fields (1 hz to 100 khz) *Health Phys.* **99** 818–36

[3] Garraud A, Jimenez J D, Garraud N and Arnold D P 2014 Electrodynamic wireless power transmission to rotating magnet receivers *J. Phys.: Conf. Ser.* **557** 012136

[4] Truong B D and Roundy S 2018 Wireless power transfer system with center-clamped magneto-mechano-electric (MME) receiver: model validation and efficiency investigation *Smart Mater. Struct.* **28** 015004

[5] Truong B D, Williams S and Roundy S 2019 Experimentally validated model and analytical investigations on power optimization for piezoelectric-based wireless power transfer systems *J. Intell. Mater. Syst. Struct.* **30** 2464–77

[6] Garraud N, Garraud A, Munzer D, Althar M and Arnold D P 2019 Modeling and experimental analysis of rotating magnet receivers for electrodynamic wireless power transmission *J. Phys. D: Appl. Phys.* **52** 185501

[7] IEEE 2006 IEEE standard for safety levels with respect to human exposure to radio frequency electromagnetic fields, 3 khz to 300 ghz *IEEE Std C95.1-2005 (Revision of IEEE Std C95.1-1991)* 1–238

[8] Lee S, Su M Y, Liang M, Chen Y, Hsieh C, Yang C, Lai H, Lin J and Fang Q 2011 A programmable implantable microstimulator soc with wireless telemetry: Application in closed-loop endocardial stimulation for cardiac pacemaker *IEEE Trans. Biomed. Circuits Syst.* **5** 511–22

[9] Monti G, Arcuti P and Tarricone L 2015 Resonant inductive link for remote powering of pacemakers *IEEE Trans. Microw. Theory Tech.* **63** 3814–22

[10] Campi T, Cruciani S, Palandrani F, De Santis V, Hirata A and Feliziani M 2016 Wireless power transfer charging system for aimds and pacemakers *IEEE Trans. Microw. Theory Tech.* **64** 633–42

[11] McRobbie D 2011 Concerning guidelines for limiting exposure to time-varying electric, magnetic and electromagnetic fields (1 hz-100 khz) *Health Phys.* **100** 04

[12] Basaeri H, Christensen D B and Roundy S 2016 A review of acoustic power transfer for bio-medical implants, *Smart Mater. Struct.* **25** 123001

[13] Ortega N, Kumar A, Scott J F and Katiyar R S 2015 Multifunctional magnetoelectric materials for device applications *J. Phys.: Condens. Matter.* **27** 504002

[14] Spaldin N A and Ramesh R 2019 Advances in magnetoelectric multiferroics *Nat. Mater.* **18** 203–12

[15] Nan T *etal* 2017 Acoustically actuated ultra-compact nems magnetoelectric antennas *Nat. Commun.* **8** 12

[16] Röntgen W C 1888 Ueber die durch bewegung eines im homogenen electrischen felde befindlichen dielectricums hervorgerufene electrodynamische kraft *Ann. Phys., Lpz.* **271** 264–70

[17] Debye P 1926 Bemerkung zu einigen neuen versuchen über einen magneto-elektrischen richteffekt *Z. für Phys.* **36** 300–1

[18] van Suchtelen J 1972 Product properties: A new application of composite materials *Philips Res. Rep.* **27** 28–37

[19] Ryu J, Carazo A V, Uchino K and Kim H-E 2001 Magnetoelectric properties in piezoelectric and magnetostrictive laminate composites *Japan. J. Appl. Phys.* **40** 4948–51

[20] Dong S, Li J-F and Viehland D 2003 Longitudinal and transverse magnetoelectric voltage coefficients of magnetostrictive/piezoelectric laminate composite: theory *IEEE Trans. Ultrason. Ferroelectr. Freq. Control* **50** 1253–61

[21] Dong S, Jie-Fang Li and Viehland D 2004 Longitudinal and transverse magnetoelectric voltage coefficients of magnetostrictive/ piezoelectric laminate composite: experiments *IEEE Trans. Ultrason. Ferroelectr. Freq. Control* **51** 794–9

[22] Gao J, Gray D, Shen Y, Li J and Viehland D 2011 Enhanced dc magnetic field sensitivity by improved flux concentration in magnetoelectric laminates *Appl. Phys. Lett.* **99** 153502

[23] Wang Y, Li M, Hasanyan D, Gao J, Li J and Viehland D 2012 Geometry-induced magnetoelectric effect enhancement and

noise floor reduction in metglas/piezofiber sensors *Appl. Phys. Lett.* **101** 092905
[24] Wang Z *et al* 2016 Highly sensitive flexible magnetic sensor based on anisotropic magnetoresistance effect *Adv. Mater.* **28** 9370–7
[25] Gajek M, Bibes M, Fusil S, Bouzehouane K, Fontcuberta J, Barthèlèmy A and Fert A 2007 Tunnel junctions with multiferroic barriers *Nat. Mater.* **6** 296–302
[26] Yang F, Zhou Y C, Tang M H, Liu F, Ma Y, Zheng X J, Zhao W F, Xu H Y and Sun Z H 2009 Eight-logic memory cell based on multiferroic junctions *J. Phys. D: Appl. Phys.* **42** 072004
[27] Hu J-M, Li Z, Chen L-Q and Nan C-W 2011 High-density magnetoresistive random access memory operating at ultralow voltage at room temperature *Nat. Commun.* **2** 553
[28] Geiler A L *et al* 2010 Multiferroic heterostructure fringe field tuning of meander line microstrip ferrite phase shifter *Appl. Phys. Lett.* **96** 053508
[29] Lee J, Hong Y-K, Lee W, Abo G S, Park J, Neveu N, Seong W-M, Park S-H and Ahn W-K 2012 Soft m-type hexaferrite for very high frequency miniature antenna applications *J. Appl. Phys.* **111** 07A520
[30] Liu M, Howe B M, Grazulis L, Mahalingam K, Nan T, Sun N X and Brown G J 2013 Voltage-impulse-induced non-volatile ferroelastic switching of ferromagnetic resonance for reconfigurable magnetoelectric microwave devices *Adv. Mater.* **25** 4886–92
[31] O'Handley R C, Huang J K, Bono D C and Simon J 2008 Improved wireless, transcutaneous power transmission for in vivo applications *IEEE Sens.* J. **8** 57–62
[32] Newacheck S and Youssef G 2019 Wireless energy transfer based on strain-mediated composite multiferroics, *Smart Mater. Struct.* **29** 015014
[33] Leung C M, Li J, Viehland D and Zhuang X 2018 A review on applications of magnetoelectric composites: from heterostructural uncooled magnetic sensors, energy harvesters to highly efficient power converters *J. Phys. D: Appl. Phys.* **51** 263002
[34] Chu Z, PourhosseiniAsl M and Dong S 2018 Review of multi-layered magnetoelectric composite materials and devices applications *J. Phys. D: Appl. Phys.* **51** 243001
[35] Cheng Y, Peng B, Hu Z, Zhou Z and Liu M 2018 Recent development and status of magnetoelectric materials and devices *Phys. Lett.* **382** 3018–25
[36] Sirohi J and Chopra I 2000 Fundamental understanding of piezoelectric strain sensors *J. Intell. Mater. Syst. Struct.* **11** 246–57
[37] Bichurin M I, Petrov V M and Srinivasan G 2002 Theory of low-frequency magnetoelectric effects in ferromagnetic-ferroelectric layered composites *J. Appl. Phys.* **92** 7681–3
[38] Osaretin I A and Rojas R G 2010 Theoretical model for the magnetoelectric effect in magnetostrictive/piezoelectric composites *Phys. Rev.* B **82** 174415 p
[39] Subhani S M, Chelvane J A and Arockiarajan A 2018 Experimental investigation of performance of tri-layered magnetoelectric composites under thermal environment *J. Phys. D: Appl. Phys.* **51** 295001
[40] Bian L, Wen Y, Li P, Gao Q and Zheng M 2009 Magnetoelectric transducer with high quality factor for wireless power receiving *Sensors Actuators A: Phys.* **150** 207–11
[41] Wang Y, Hasanyan D, Li M, Gao J, Li J, Viehland D and Luo H 2012 Theoretical model for geometry-dependent magnetoelectric effect in magnetostrictive/piezoelectric composites *J. Appl. Phys.* **111** 124513
[42] Jorge Nocedal S W 2006 *Numerical Optimization* (New York: Springer)
[43] Domann J P, Loeffler C M, Martin B E and Carman G P 2015 High strain-rate magnetoelasticity in galfenol *J. Appl. Phys.* **118** 123904
[44] Summers E, Meloy, R and Restorff J B 2009 Galfenol alloying additions and the effects on uniaxial anisotropy generation *J. Appl. Phys.* **106** 024914
[45] Chang C-M and Carman G P 2007 Experimental evidence of end effects in magneto-electric laminate composites *J. Appl. Phys.* **102** 124901
[46] Zhao C P, Fang F and Yang W 2010 A dual-peak phenomenon of magnetoelectric coupling in laminated terfenol-d/PZT/terfenol-d composites, *Smart Mater. Struct.* **19** 125004
[47] Zhou H-M, Li M-H, Li X-H and Zhang D-G 2016 An analytical and explicit multi-field coupled nonlinear constitutive model for terfenol-d giant magnetostrictive material *Smart Mater. Struct.* **25** 085036
[48] Kurs A, Karalis A, Moffatt R, Joannopoulos J D, Fisher P and Soljačić M 2007 Wireless power transfer via strongly coupled magnetic resonances *Science* **317** 83–6
[49] Moore J, Castellanos S, Xu S, Wood B, Ren H and Tse Z T H 2018 Applications of wireless power transfer in medicine: State-of-the-art reviews *Ann. Biomed. Eng.* **47** 22–38
[50] Schormans M, Valente V and Demosthenous A 2018 Practical inductive link design for biomedical wireless power transfer: A tutorial *IEEE Trans. Biomed. Circuits Syst.* **12** 1112–30
[51] Ahn D and Ghovanloo M 2016 Optimal design of wireless power transmission links for millimeter-sized biomedical implants *IEEE Trans. Biomed. Circuits Syst.* **10** 125–37
[52] Silay K M, Dehollain C and Declercq M 2011 Inductive power link for a wireless cortical implant with two-body packaging *IEEE Sens.* J. **11** 2825–33
[53] Poon A S Y, O'Driscoll S and Meng T H Optimal frequency for wireless power transmission into dispersive tissue *IEEE Trans. Antennas Propag.* **58** 1739–50 2010
[54] Ho J S, Yeh A J, Neofytou E, Kim S, Tanabe Y, Patlolla B, Beygui R E and Poon A S Y 2014 Wireless power transfer to deep-tissue microimplants *Proc. Natl Acad. Sci.* **111** 7974–9
[55] Mazzilli F, Lafon C and Dehollain C 2014 A 10.5 cm ultrasound link for deep implanted medical devices *IEEE Trans. Biomed. Circuits Syst.* **8** 738–50
[56] Basaeri H, Yu Y, Young D and Roundy S 2019 A mems-scale ultrasonic power receiver for biomedical implants *IEEE Sensors Lett.* **3** 1–4